

# Best practices for velocity estimations in highly aerated flows with dual-tip phase-detection probes

M. Kramer<sup>a,\*</sup>, B. Hohermuth<sup>b</sup>, D. Valero<sup>c</sup>, S. Felder<sup>d</sup>

<sup>a</sup>*UNSW Canberra, School of Engineering and Information Technology (SEIT), Canberra, ACT 2610, Australia, m.kramer@adfa.edu.au, ORCID 0000-0001-5673-2751*

<sup>b</sup>*Laboratory of Hydraulics, Hydrology and Glaciology (VAW), ETH Zurich, Switzerland, hohermuth@vaw.baug.ethz.ch, ORCID 0000-0001-8218-0444*

<sup>c</sup>*IHE Delft Institute for Water Education, Water Resources and Ecosystems, 2611 AX Delft, the Netherlands, d.valero@un-ihe.org, ORCID 0000-0002-7127-7547*

<sup>d</sup>*Water Research Laboratory, School of Civil and Environmental Engineering, UNSW Sydney, NSW 2052, Australia, s.felder@unsw.edu.au, ORCID 0000-0003-1079-6658*

---

## Abstract

Dual-tip phase-detection probes can be used to measure flow properties in gas-liquid flows. Traditionally, time-averaged interfacial velocities have been obtained through cross-correlation analysis of long time-series of phase fraction signals. Using small groups of detected particles, a recently developed adaptive window cross-correlation (AWCC) technique enables the computation of pseudo-instantaneous interfacial velocities and turbulence quantities in highly aerated flows, albeit subject to some smoothing which is due to the use of a finite window duration. This manuscript provides guidance on the selection of optimum processing parameters for the AWCC technique, additionally addressing shortcomings such as velocity bias correction in turbulent flows and extrapolation of turbulence levels to single particles. The presented technique was tested for three highly turbulent air-water flows: smooth and rough-wall boundary layers (tunnel chute and stepped spillway), as well as breaking shear layer flows of a hydraulic jump. Robust estimations of mean velocities and velocity fluctuations were obtained for all flow situations, either using dual-tip conductivity or fiber optical probe data. The computation of integral time scales and velocity spectra is currently limited by the data rate and must be treated with caution.

---

\*Corresponding author

*Keywords:* Dual-tip phase-detection probe, signal processing, adaptive window cross-correlation (AWCC), gas-liquid flows, multiphase flow turbulence

---

## 1. Introduction

*White waters* can be observed in free-surface flows such as hydraulic jumps or high-speed flows over smooth or rough beds. Aerated flows present a complex structure (Wilhelms and Gulliver, 2005) and its inception is strongly linked to the presence of turbulence close to the free-surface (Brocchini and Peregrine, 2001; Valero and Bung, 2018b). Entrained air limits the use of common monophasic flow measurement methods and has motivated the development of specialised air-water flow instrumentation (Jones and Delhay, 1976; Van der Welle, 1985; Kataoka et al., 1986; Revankar and Ishii, 1993; Crowe et al., 2011).

Dual-tip phase-detection probes (figure 1a) have been used to measure air-water flow properties intrusively since the early works of Neal and Bankoff (1963) and Heringe and Davis (1976). A single-threshold technique (Cartellier and Achard, 1991; Felder and Chanson, 2015) is typically used to analyse the raw voltage signal of the probe  $S(\mathbf{x}, t)$  (figure 1b,c), providing an ideal square wave time series of instantaneous void fractions, with  $c(\mathbf{x}, t) = 1$  for air and  $c(\mathbf{x}, t) = 0$  for water. From the instantaneous void fraction signal, time-averaged void fraction  $C(\mathbf{x})$ , time-averaged particle count rate  $F(\mathbf{x})$  and chord times can be deduced (Chanson, 2016). Note that  $\mathbf{x}$  refers to the spatial coordinate of the leading tip of the probe and  $t$  refers to the time coordinate. For the sake of conciseness,  $\mathbf{x}$  is dropped from the following analysis, although flow dependent variables can naturally vary across space.

### 1.1. Conventional velocity and turbulence level estimations

Velocity fluctuations in bubbly flows were investigated by Sene (1984); Cartellier (1992, 1998); Serdual and Loewen (1998), using the phase function gradients of a single-tip fiber optical (FO) signal. Similarly, Chang et al. (2003) and Zhang et al. (2014) used event detection techniques to measure bubble velocities with a single-tip fiber optical probe. While these techniques are applicable for finely dispersed flows, dual-tip probes are better suited to cover a wide range of void fractions (Chanson, 2002, 2016; Valero and Bung, 2018a), which can be common in free-surface air-water flows.

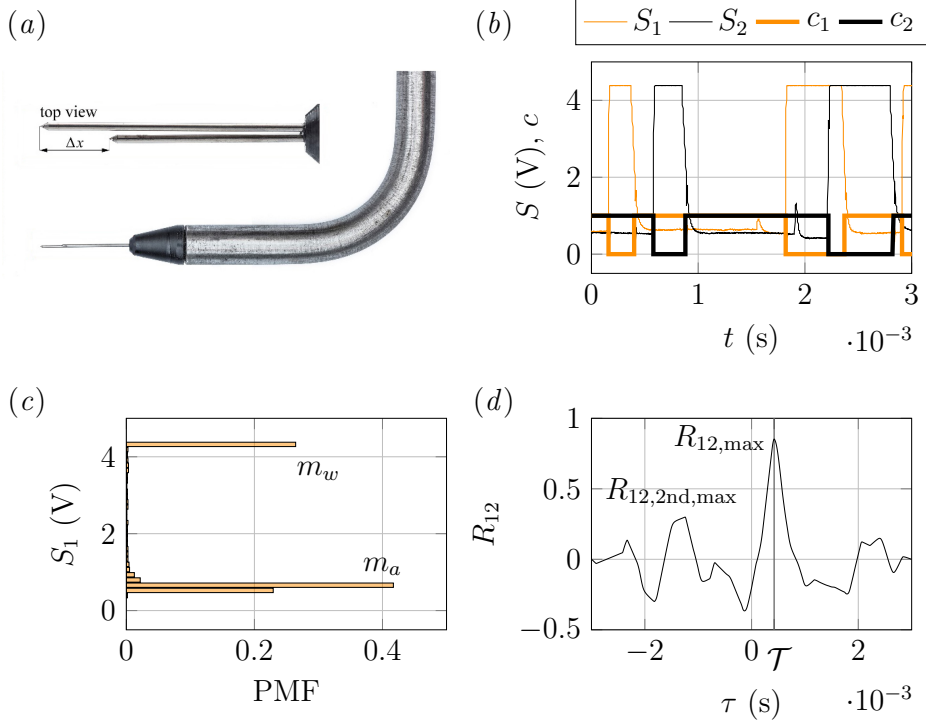


Figure 1: Phase-detection probe design and recorded signals: (a) dual-tip phase-detection conductivity probe (CP) (b) typical leading and trailing tip raw voltage signal ( $S_1$ ,  $S_2$ ) and instantaneous void fraction ( $c_1$ ,  $c_2$ ); tunnel chute data with  $C \approx 0.6$  (c) probability mass function (PMF) of the raw voltage signal with  $m_w$ ,  $m_a =$  mode of the water and air phase, respectively (d) cross-correlation function  $R_{12}$  versus time lag  $\tau$ , with  $R_{12,\max} = 0.85$  and secondary peak ratio  $\text{SPR} = R_{12,2\text{nd},\max}/R_{12,\max} \approx 0.45$ ;  $\mathcal{T}$  = interfacial travel time.

The estimation of the local time-averaged interfacial velocities with dual-tip phase-detection probes is based upon the cross-correlation analysis of the simultaneously sampled signals of the two probe tips.

The cross-correlation can provide the time shift between the probe tip signals (Cain and Wood, 1981; Chanson, 2002; Crowe et al., 2011), i.e. the most probable time lag ( $\mathcal{T}$ ) between a pair of phase functions. Knowing the streamwise distance between the probe tips ( $\Delta x$ ), the expected value of the mean interfacial velocity can be obtained as:

$$\langle U \rangle \approx \frac{\Delta x}{\mathcal{T}} \quad (1)$$

Here the operator  $\langle \dots \rangle$  denotes time-averaging. Chanson and Toombes (2002) suggested that indirect turbulence estimations could be obtained on the basis of the standard deviation of the auto- and cross-correlation functions ( $\sigma_{11}$  and  $\sigma_{12}$ ) of the raw phase-detection probe signal ( $S_1, S_2$ ):

$$Tu = u_{rms}/\langle U \rangle \approx \sqrt{\sigma_{12}^2 - \sigma_{11}^2}/\mathcal{T} \quad (2)$$

Based on eq. (2), any imperfections that imply a decorrelation between  $S_1$  and  $S_2$  can result in a higher turbulence level, which may not be related to the flow properties but to experimental defects. Apart from actual turbulent velocity fluctuations, several effects could cause a reduction in the correlation of the two signals, including 1) sampling rate: only an infinite sampling rate would yield a perfect correlation 2) transversal tip separation: the transverse separation leads to different chord times of the leading and trailing tips, resulting in a loss of correlation 3) probe misalignment 4) particle-probe interactions: the deformation of an air or water particle during the piercing of a probe tip leads to a lower correlation because the trailing tip detects a differently shaped particle.

### 1.2. Adaptive window cross-correlation (AWCC) technique

Recently, Kramer et al. (2019) developed an adaptive window cross-correlation (AWCC) technique for processing dual-tip phase-detection probe signals. The AWCC Matlab source code is available on GitHub (Kramer and Valero, 2019a). The main innovation of the AWCC technique is the segmentation of dual-tip phase-detection probe signals into very short windows (such as those in figure 1b) and the subsequent estimation of a pseudo-instantaneous velocity for each window. The window duration is determined upon a defined number of dispersed phase particles ( $N_p$ ) contained in a given segment. Each particle is defined as a pair of interfaces; for instance, the leading and the trailing tip signals shown in figure 1b contain two dispersed phase particles each.

The segmentation of the signal into a series of windows provides a time series of pseudo-instantaneous interfacial velocities ( $U(t)$ ) in highly aerated flows, enabling a direct computation of turbulence parameters. Here, the term *pseudo*-instantaneous is used because each velocity estimation is representative of a number of  $N_p$  particles, i.e. it is averaged over the window duration. It is expected that instantaneous velocity estimations can be obtained on the limit  $N_p \rightarrow 1$ . The AWCC was validated by stochastic modelling, showing that the method is accurate, although it was noticed that

the uncertainty (e.g. velocity bias) may increase with increasing velocity fluctuations (Kramer et al., 2019).

Experimentally recorded signals are different from synthetic signals and the utilization of the AWCC technique in laboratory or large-scale applications requires an appropriate selection of processing parameters, including the number of particles  $N_p$  and threshold values for the maximum cross-correlation coefficient and the secondary peak ratio (Kramer et al., 2019) (figure 1*d*). To facilitate the selection of processing parameters, this work explores the sensitivity of the AWCC technique through a re-analysis of previous phase-detection probe measurements (Felder and Pfister, 2017; Felder et al., 2019; Montano, 2019). The AWCC technique is detailed in section 2, followed by a description of the selected datasets (section 3) and a presentation of the sensitivity analysis (section 4). In section 5, the AWCC technique is compared to conventional signal processing approaches and best practices are discussed.

### 1.3. A glimpse on measurement accuracy

The performance of phase-detection probes has been addressed by several researchers (table 1). A conclusive statement on the measurement uncertainty is challenging, given the variety of probe designs and flow conditions. Table 1 summarises previous literature on the accuracy of void fraction  $C$  and interfacial velocity  $\langle U \rangle$ .

Table 1: Reported measurement uncertainties for phase-detection probe data; CP: phase-detection conductivity probe; FO: phase-detection fiber optical probe.

Reference	$\Delta C/C$	$\Delta \langle U \rangle / \langle U \rangle$	comment	probe
Cummings and Chanson (1997)	$\approx \pm 0.001/C$	$\pm 10\%$	$C < 0.05$	dual-tip CP
Cummings and Chanson (1997)	$\pm 2\%$	$\pm 5\%$	$0.05 < C < 0.95$	dual-tip CP
Cummings and Chanson (1997)	$\approx \pm 0.001/(1 - C)$	$\pm 10\%$	$C > 0.95$	dual-tip CP
Barrau et al. (1999)	0% to $-16\%$		bubbly flow	dual-tip FO
Boes (2000)	$< -5\%$	$< \pm 5\%$	highly aerated flow	dual-tip FO
Kiambi et al. (2003)	$-6\%$ to $-14\%$	$< +5\%$	bubbly flow	dual-tip FO
Cartellier (2006)	$< -5\%$	$< 5\%$	thin and sharp tip	dual-tip FO
Vejrazka et al. (2010)	$-10\%$		bubbly flow correction applied	single-tip FO

The phase-detection probes of the studies re-analysed in this manuscript compared well with other conductivity probes (e.g. Cummings and Chanson, 1997) and fiber optical probes (e.g. Boes, 2000), as shown in Felder and Pfister (2017); Felder et al. (2019). The measurement uncertainty of the conductivity probes in this manuscript is therefore expected to be similar to the data presented in table 1. Additional uncertainty may be linked to sampling parameters as shown for the sampling duration in Appendix A.

## 2. Signal processing

The processing steps of the AWCC technique involve the calculation of basic multiphase flow parameters (void fraction, chord times, particle count rate), segmentation of the signal into adaptive windows, filtering and calculation of pseudo-instantaneous interfacial velocities (figure 2). Further analyses on the obtained velocity time series are presented in section 2.4.

### 2.1. Void fraction and particle count rate

The raw signals of the leading ( $S_1$ ) or trailing tip ( $S_2$ ) of a phase-detection probe often differ from an ideal square-wave signal because of wetting and drying processes and electrical noise (figure 1b). Therefore, single-threshold (Cartellier and Achard, 1991; Toombes, 2002; Felder and Chanson, 2015) or double-threshold techniques (Van der Welle, 1985; Wang et al., 2017) are commonly used to obtain the instantaneous void fraction  $c(t)$ . For the leading tip signal, a single-threshold criteria based on 50 % of the intermodal voltage range can be written as:

$$\frac{S_1(t) - m_a}{(m_w - m_a)} \begin{cases} \geq 0.5 \rightarrow c_1(t) = 0 \\ < 0.5 \rightarrow c_1(t) = 1 \end{cases} \quad (3)$$

where  $m_w$  and  $m_a$  are the modes of the probability mass function of the raw signal (figure 1c), corresponding to the water and air phases respectively. The time averaged void fraction  $C$  is calculated as:

$$C = \frac{1}{T} \int_{t=0}^T c_1(t) dt \quad (4)$$

where the sampling duration  $T$  is significantly larger than the time scale of turbulent processes.

The instantaneous void fraction can provide air and water chord times ( $t_{ch,a}$  and  $t_{ch,w}$ ), the total number of particles in the signal  $N$  (equal to half the number of detected interfaces) and the time-averaged particle count rate can be estimated as:

$$F = \frac{N}{T} \quad (5)$$

## 2.2. Signal segmentation

The adaptive window duration  $\mathcal{W}_T$  is determined to enclose a certain number of individual bubble-droplet events (Kramer et al., 2019). Given the air and water chord times, the start and end times for the  $i^{th}$  window are determined on the basis of the leading tip signal ( $S_1$ ) and a selected number of particles  $N_p$ . The start time of the first window is  $t_{s,1} = 0$  and the start times for  $2 \leq i \leq n_{\mathcal{W}}$  are computed as:

$$t_{s,i} = \sum_{j=1}^{N_p \cdot (i-1)} t_{ch,a,j} + \sum_{j=1}^{N_p \cdot (i-1)} t_{ch,w,j} \quad \{i \in \mathbb{Z}^+ : 2 \leq i \leq n_{\mathcal{W}}\} \quad (6)$$

where  $n_{\mathcal{W}} = \lfloor N/N_p \rfloor$  is the number of windows and  $\lfloor \cdot \rfloor$  is the floor function. The end times read:

$$t_{e,i} = \sum_{j=1}^{N_p \cdot i} t_{ch,a,j} + \sum_{j=1}^{N_p \cdot i} t_{ch,w,j} \quad \{i \in \mathbb{Z}^+ : 1 \leq i \leq n_{\mathcal{W}}\} \quad (7)$$

Equations (6) and (7) imply that each segment of the leading tip signal ( $S_1$ ) contains  $N_p$  particles, whereas the number of particles in the trailing tip signal ( $S_2$ ) can be different. The window duration for the  $i^{th}$  window is:

$$\mathcal{W}_{T,i} = t_{e,i} - t_{s,i} \quad (8)$$

It is further assumed that the time  $t_i$  of the velocity estimation is represented by the midpoint:

$$t_i = (t_{s,i} + t_{e,i})/2 \quad (9)$$

and the signals contained in the  $i^{th}$  window are:

$$S_{1,i} = S_1(t_{s,i} \leq t \leq t_{e,i}), \quad S_{2,i} = S_2(t_{s,i} \leq t \leq t_{e,i}) \quad (10)$$

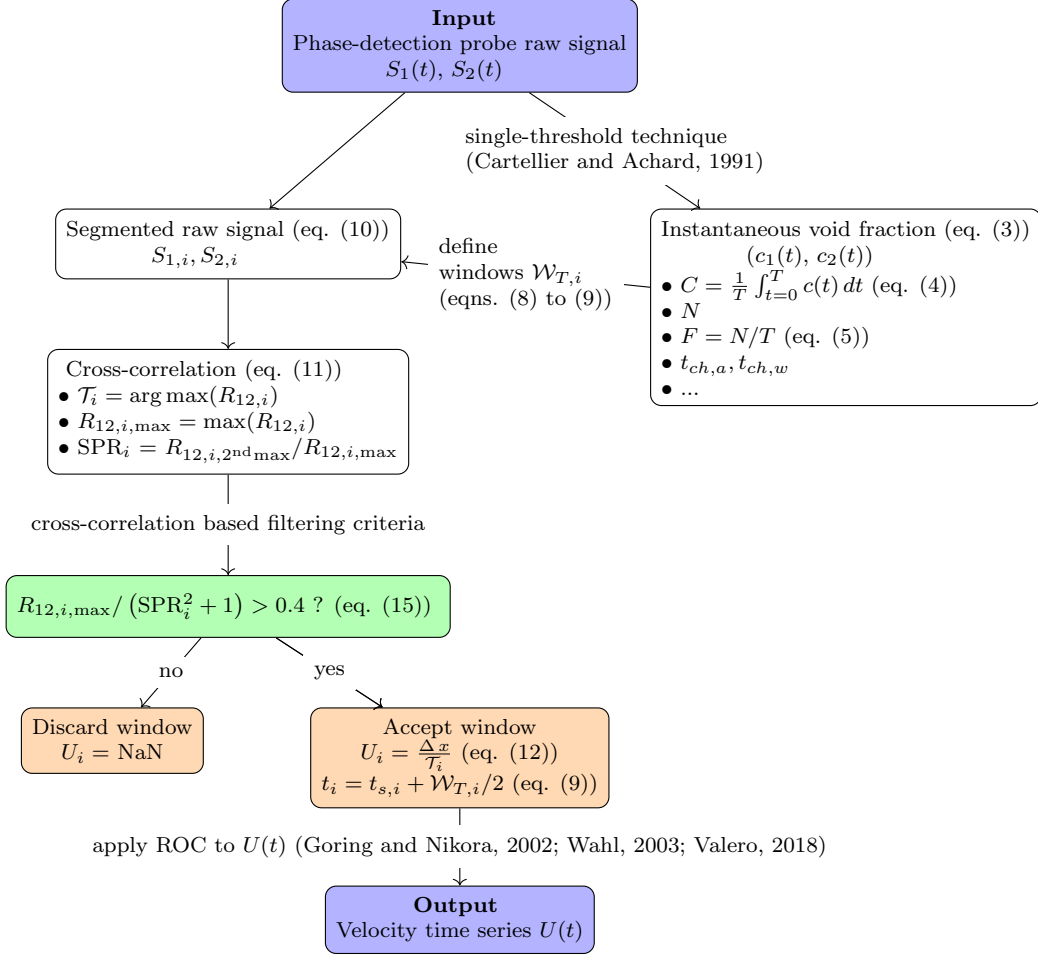


Figure 2: Flowchart of the AWCC technique for dual-tip phase-detection probe data; ROC: Robust Outlier Cutoff; NaN: Not a Number.

### 2.3. Velocity estimation and filtering

The interfacial travel time for an arbitrary window is obtained by means of the cross-correlation of the leading and trailing tip signals:

$$R_{12,i}(\tau) = \frac{\sum_{t=t_{s,i}}^{t_{s,i}+W_{T,i}} \left( [S_1(t) - \langle S_{1,i} \rangle] \cdot [S_2(t+\tau) - \langle S_{2,i} \rangle] \right)}{\sqrt{\sum_{t=t_{s,i}}^{t_{s,i}+W_{T,i}} \left( S_1(t) - \langle S_{1,i} \rangle \right)^2} \cdot \sqrt{\sum_{t=t_{s,i}}^{t_{s,i}+W_{T,i}} \left( S_2(t+\tau) - \langle S_{2,i} \rangle \right)^2}} \quad (11)$$

where  $\tau$  is the time lag and  $R_{12,i}$  the cross-correlation function. The peak of  $R_{12,i}$  indicates the interfacial travel time  $\mathcal{T}_i (= \arg \max(R_{12,i}))$  for which both

signals are best correlated (figure 1d). A longitudinal pseudo-instantaneous velocity is estimated through eq. (1) for each window as:

$$\left[ \langle U \rangle \right]_{t_{s,i}}^{t_{s,i} + \mathcal{W}_{T,i}} \approx U_i = \frac{\Delta x}{\mathcal{T}_i} \quad (12)$$

Shortcomings can be caused by oblique particle impacts, resulting in large velocities due to a nearly simultaneous recording of interfaces at both tips (Thorwarth, 2008), or by windows capturing different particle events; while the cross-correlation functions appear reasonable, the interfacial velocity could be overestimated.

To limit erroneous velocity estimations, a robust filtering approach was proposed by Kramer et al. (2019), comprising thresholds for 1) the maximum cross-correlation coefficient  $R_{12,i,\max}$ , representing the similarity between  $S_{1,i}$  and  $S_{2,i}$  and 2) the secondary peak ratio  $\text{SPR}_i = R_{12,i,2\text{nd},\max} / R_{12,i,\max}$ .  $\text{SPR}_i$  is defined as the ratio of the second tallest peak to the first tallest peak of the cross-correlation function (figure 1d) and indicates the presence of one or more events within one window. Note that both parameters detect different physical processes with the aim to characterise the *quality* of a cross-correlation function. The choice of threshold values for  $R_{12,i,\max}$  and  $\text{SPR}_i$  as well as a combined filtering criteria are discussed in section 4.1.1.

In addition to the cross-correlation based filtering, a simplified version of the despiking method proposed by Goring and Nikora (2002), as modified by Wahl (2003), is applied to the estimated velocity time series  $U_i$  at  $t_i$ . The Robust Outlier Cutoff (ROC, see Valero, 2018) is performed iteratively until no more outliers are rejected. Outliers are accounted as NaN data.

#### 2.4. Time series analysis

Similar to time series obtained with laser Doppler anemometers (LDA), phase-detection probe velocity measurements  $U(t)$  may overestimate the mean velocity because more particles pass the measurement volume/hit the probe tips at higher velocities (Britz and Antonia, 1996; Kramer et al., 2019). This shift of the mean velocity towards a higher value is known as velocity bias (McLaughlin and Tiederman, 1973). Herein, the following correction was used to eliminate the velocity bias for phase-detection probe measurements:

$$\langle U \rangle = \frac{\sum_{i=1}^{n_{\mathcal{W}}} w_i U_i}{\sum_{i=1}^{n_{\mathcal{W}}} w_i} \quad (13)$$

$$u_{rms} = \sqrt{\frac{\sum_{i=1}^{n_W} (U_i - \langle U \rangle)^2 w_i}{\sum_{i=1}^{n_W} w_i}} \quad (14)$$

where  $w_i$  is a weighting factor and the summations are taken over the entire ensemble. Common weighting schemes for LDA measurements comprise inverse absolute velocity weighting (McLaughlin and Tiederman, 1973), particle interarrival time weighting (Hoesel and Rodi, 1977) and particle residence time weighting (Buchhave et al., 1979), where the latter is the most appropriate method to eliminate velocity bias in LDA data (Velte et al., 2014).

As residence times are not available for air-water flow data, the synthetic signals of Kramer et al. (2019) were re-analysed and three different weighting schemes for the AWCC technique were tested. In Kramer et al. (2019), a virtual dual-tip phase-detection probe was immersed in a pattern of randomly distributed fluid particles (following a gamma distribution with 3 mm mean diameter), simulating 1D turbulent motion. The tip separation was  $\Delta x = 4$  mm and the probe was sampled for  $T = 10$  s at  $f = 20$  kHz, generating instantaneous void fraction signals. Additional information on synthetic signals and the stochastic particle generator can be found in Valero et al. (2019); Kramer (2019).

Table 2: Comparison of different weighting schemes using synthetic signals; turbulence level  $Tu = u_{rms}/\langle U \rangle$ ; integral time scale  $T_{uu} = 0.06$  s for all flow conditions; data processed with  $N_p = 2$  and errors calculated as  $e_{\langle U \rangle} = (\langle U \rangle - \langle U \rangle_{sim}) / \langle U \rangle_{sim}$ .

Simulation				Relative errors using different weighting schemes							
$\langle U \rangle_{sim}$ (m/s)	$Tu_{sim}$ (-)	$C_{sim}$ (-)	$F$ (1/s)	$e_{\langle U \rangle}$ (%)	$e_{Tu}$ (%)	$e_{\langle U \rangle}$ (%)	$e_{Tu}$ (%)	$e_{\langle U \rangle}$ (%)	$e_{Tu}$ (%)	$e_{\langle U \rangle}$ (%)	$e_{Tu}$ (%)
				no weighting	1/ U <sub>i</sub>		$t_i - t_{i-1}$		$\mathcal{W}_{T,i}$		
3.0	0.1	0.3	142	0.9	-1.9	0.4	0.8	0.6	1.0	0.6	1.0
3.0	0.1	0.1	56	1.4	-2.3	1.5	0.0	1.8	-3.2	1.8	-5.6
3.0	0.2	0.3	140	3.0	-9.5	0.3	-4.1	1.2	-5.5	1.2	-6.3
3.0	0.2	0.1	57	3.8	-10.0	1.1	-8.5	1.8	-12.4	1.5	-7.9
3.0	0.3	0.3	144	7.6	-11.7	0.3	-0.9	2.0	-5.5	1.1	-5.2
3.0	0.4	0.3	131	19.0	-23.9	3.7	-10.6	6.2	-15.5	4.5	-14.0
3.0	0.5	0.3	143	28.7	-33.2	7.5	-15.9	11.9	-22.7	9.0	-19.3

To determine the best weighting scheme for the AWCC technique, the synthetic void fraction signals were re-analysed using 1) inverse absolute ve-

locity weighting ( $w_i = 1/|U_i|$ ), 2) interarrival time weighting ( $w_i = t_i - t_{i-1}$ ) and 3) window duration weighting ( $w_i = \mathcal{W}_{T,i}$ ). The results were compared with arithmetic statistics ( $w_i = 1$ , no weighting), highlighting that all weighting schemes reduced the errors in terms of mean velocities and velocity fluctuations (table 2). Despite having the lowest errors for the investigated 1D synthetic signals, inverse velocity weighting led to unreasonable mean velocities in free shear regions (e.g. in hydraulic jumps), possibly caused by the assignment of very large weights to near-zero velocities. Interarrival time weighting and window duration weighting performed comparably. Hereafter, mean velocities  $\langle U \rangle$  and *rms* velocity fluctuations  $u_{rms}$  were evaluated using equations (13) and (14) with  $w_i = \mathcal{W}_{T,i}$  (window duration weighting).

Further quantities of interest include turbulent properties such as the auto-correlation function (ACF) and the power spectral density (PSD). When calculating these properties from AWCC (likewise LDA) velocity time series, the effect of non-uniform sampling must be considered. Benedict et al. (2000) and Damaschke et al. (2018) compared state-of-the-art ACF and PSD estimation methods for LDA data, for example slotting and interpolation techniques. In the present study, nearest-neighbor (NN) resampling and autoregressive moving-average (ARMA) model fitting (Broersen et al., 2000) was used for the AWCC technique to estimate ACF and PSD. NN resampling was performed at twice the mean data rate ( $f_m$ ) of the original time series, where  $f_m$  is defined as the amount of valid velocity information per time. This method allows spectral estimates up to  $0.5f_m$ .

### 3. Datasets and experimental facilities

#### 3.1. General remarks

Three datasets comprising high-velocity air-water flows down a stepped spillway (figure 3.1a), high-velocity air-water flows in a smooth tunnel chute (figure 3.1b) and a fully aerated hydraulic jump (figure 3.1c) were re-analysed with the AWCC. In all datasets, dual-tip phase-detection intrusive probes were used, comprising conductivity probes (CP) manufactured in the Water Research Laboratory (WRL, UNSW Sydney) (figure 1a) and a commercial fiber optical (FO) probe from RBI.

All dual-tip probes had a side-by-side design, as recommended by Felder et al. (2019). The conductivity probes were similar, with inner electrodes of platinum wire ( $\phi = 0.125$  mm) and outer electrodes of hypodermic needles ( $\phi = 0.6$  mm); both electrodes were insulated using epoxy. Every time an air

entity is pierced by a probe tip, the voltage signal drops to about 0.5 V and when a probe tip is in water, the voltage signal increases to about 4.1 V (figure 1*b*). The fiber optical probe tips record the air-water phases via a change in light refraction in front of the needle tips. For each dataset, the longitudinal separation distance between the leading and trailing tips  $\Delta x$ , the sampling time  $T$ , the sampling rate  $f$  and the Reynolds number are provided in table 3. The choice of the sampling parameters fulfilled the requirements set by earlier sensitivity analyses (Felder and Chanson, 2015). A convergence analysis of the stepped spillway data showed that sampling durations  $T > 45$  s could further improve the measurement accuracy (Appendix A). The raw voltage signals were recorded with the same LabVIEW-based data acquisition system using a high-speed acquisition unit (National Instruments USB-6366) and further details on the overall probe designs can be found in Felder and Pfister (2017) and Felder et al. (2019).

Table 3: Experimental flow condition and dual-tip phase-detection probe specifications for the re-analysed datasets; CP: phase-detection conductivity probe; FO: phase-detection fiber optical probe; Reynolds number  $Re = q/\nu$ , with  $\nu$  the kinematic viscosity of water and  $q$  the specific discharge;  $f$ : sampling rate,  $T$ : sampling duration;  $\Delta x$ : streamwise tip separation distance.

Reference (-)	$q$ ( $\text{m}^2/\text{s}$ )	$Re$ (-)	flow type (-)	probe (-)	$f$ (kHz)	$T$ (s)	$\Delta x$ (mm)
Felder and Pfister (2017)	0.478	$1.2 \cdot 10^5$	stepped spillway	CP	500	45	5.17
Felder et al. (2019)	1.086	$1.1 \cdot 10^6$	tunnel chute	CP	500	45	5.06
Felder et al. (2019)	1.086	$1.1 \cdot 10^6$	tunnel chute	FO	500	45	5.00
Montano (2019)	0.083	$8.3 \cdot 10^4$	hydraulic jump	CP	20	300	7.9

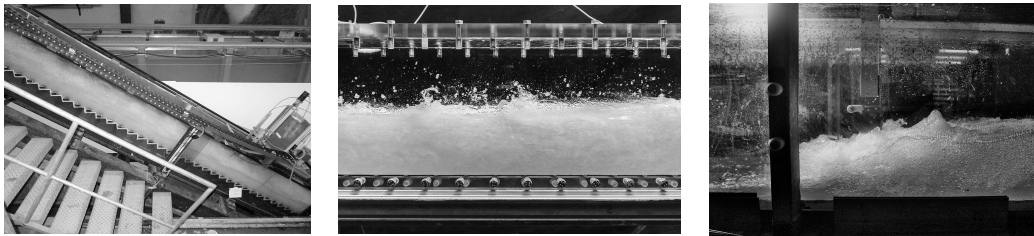


Figure 3: Case studies; flow direction from left to right (*a*, left) high-velocity flows in a stepped spillway;  $d_c/h = 9.5$ ;  $Re = 1.2 \cdot 10^5$  (*b*, middle) high-velocity flows in a tunnel chute;  $H = 15$  m;  $h_g/h_{us} = 0.4$ ;  $Re = 1.1 \cdot 10^6$  (*c*, right) fully aerated hydraulic jump;  $d_1 = 0.03$  m;  $Fr = 5.1$ ;  $Re = 8.3 \cdot 10^4$ ; photography courtesy of Laura Montano.

### 3.2. Stepped spillway (EPFL)

The stepped spillway chute (Laboratory of Hydraulic Constructions, EPFL) was 0.5 m wide, had a slope of 30 degrees and consisted of equal flat steps with height  $h = 0.03$  m. The dimensionless discharge was  $d_c/h = 9.5$  (skimming flow), where  $d_c$  is the critical flow depth. In the present study, experimental data at step edge 101 were re-analysed. Further details on the flume and the flow conditions can be found in Felder and Pfister (2017).

### 3.3. Smooth tunnel chute (ETH Zurich)

The smooth tunnel chute (Laboratory of Hydraulics, Hydrology and Glaciology, ETH Zurich) had a length of 20.6 m, a width of 0.2 m and a height of 0.3 m. The flow in the tunnel chute was controlled with a high-head sluice gate, providing high-velocity air-water flows along the tunnel chute (Felder et al., 2019). For the present re-analysis, flow conditions with an upstream head of  $H = 15$  m and relative gate opening of  $h_g/h_{us} = 0.4$  were used, where  $h_g$  is the opening height of the gate and  $h_{us}$  the flow depth upstream of the sluice gate (Hohermuth, 2019). The re-analysed phase-detection probe data were collected 17.92 m downstream of the sluice gate.

### 3.4. Hydraulic jump (UNSW Sydney)

The open channel flume (Water Research Laboratory, UNSW Sydney) used for the hydraulic jump experiments was 40 m long and 0.6 m wide. An upstream sluice gate with a rounded corner controlled supercritical flows and the longitudinal position of the hydraulic jump was adjusted with a tail gate at the end of the flume (Montano, 2019). In the present study, conductivity probe data collected at 0.24 m distance from the mean jump toe were re-analysed. The inflow was partially developed (jump toe located 0.5 m downstream of the sluice gate) with inflow depth and inflow Froude number of  $d_1 = 0.03$  m and  $Fr_1 = 5.1$ , respectively.

## 4. Results

### 4.1. Sensitivity analysis of processing parameters

The application of the AWCC technique requires the selection of processing parameters, including thresholds for  $R_{12,i,\max}$  and  $SPR_i$  and the number of particles  $N_p$ . Detailed sensitivity analyses were conducted for all data sets, providing consistent parameters irrespective of the air-water flow phenomenon. In this section, the results of the sensitivity analysis are presented for the ETH tunnel chute.

#### 4.1.1. Filtering criteria for $R_{12,i,\max}$ and $\text{SPR}_i$

Erroneous velocities can be eliminated using a cross-correlation based filtering approach with filtering thresholds  $R_{12,\text{thresh}}$  and  $\text{SPR}_{\text{thresh}}$ . These thresholds imply that velocity information is valid if  $R_{12,i,\max} > R_{12,\text{thresh}}$  and/or if  $\text{SPR}_i < \text{SPR}_{\text{thresh}}$  (Matos et al., 2002; Keane and Adrian, 1990; Kramer et al., 2019). Matos et al. (2002) and Andre et al. (2005) used  $0.5 \leq R_{12,\text{thresh}} \leq 0.7$  for phase-detection probe measurements and Keane and Adrian (1990) and Hain and Kaehler (2007) recommended  $0.5 \leq \text{SPR}_{\text{thresh}} \leq 0.8$  for particle image velocimetry (PIV).

Figure 4 shows two- and three-dimensional representations of pseudo-instantaneous  $U_i$ ,  $R_{12,i,\max}$  and  $\text{SPR}_i$  for two measurement locations next to the bed of the tunnel chute (processed with  $N_p = 6$ ), including thresholds  $R_{12,\text{thresh}} = 0.7$  (Matos et al., 2002) and  $\text{SPR}_{\text{thresh}} = 0.65$  (Keane and Adrian, 1990). The magnitude of the instantaneous velocity is plotted using a color scale and dark blue dots represent non-physical near-zero velocities (see section 4.1.2). It was observed that the secondary peak ratio ( $\text{SPR}_i$ ) was linear negatively correlated with the cross-correlation coefficient  $R_{12,i,\max}$  (figure 4). This implies that a velocity estimation with low  $R_{12,i,\max}$  has a high probability of also showing a high  $\text{SPR}_i$  value. Therefore, the use of an empirical criteria  $R_{12,i,\max} > (a \cdot \text{SPR}_i^2) + b$  is proposed, aiming to eliminate erroneous velocity estimations and to maximise the amount of accepted data through a combination of  $R_{12,i,\max}$  and  $\text{SPR}_i$  (figures 4a,b). This quadratic inequality can be simplified by setting  $a = b = \mathcal{A}$ :

$$R_{12,i,\max} / (\text{SPR}_i^2 + 1) > \mathcal{A} \quad (15)$$

where the parameter  $\mathcal{A}$  was chosen as  $\mathcal{A} = 0.4$  (figure 4). This approach implies minimum cross-correlation coefficients of  $R_{12,i,\max} > 0.4$  for  $\text{SPR}_i = 0$  and  $R_{12,i,\max} > 0.8$  for  $\text{SPR}_i = 1$  (figures 4a,b). While the lowest  $R_{12,i,\max}$  and the highest  $\text{SPR}_i$  values were – standalone – less restrictive than in previous studies (Keane and Adrian, 1990; Matos et al., 2002), the combination of both parameters provided a robust filtering approach, which was suitable for all investigated flow situations and for both, FO and CP probes. Note that  $\mathcal{A}$  in eq. (15) was selected for flow locations next to the solid boundary, representing the most challenging locations due to high turbulence levels, low void fractions and relatively low data yield.

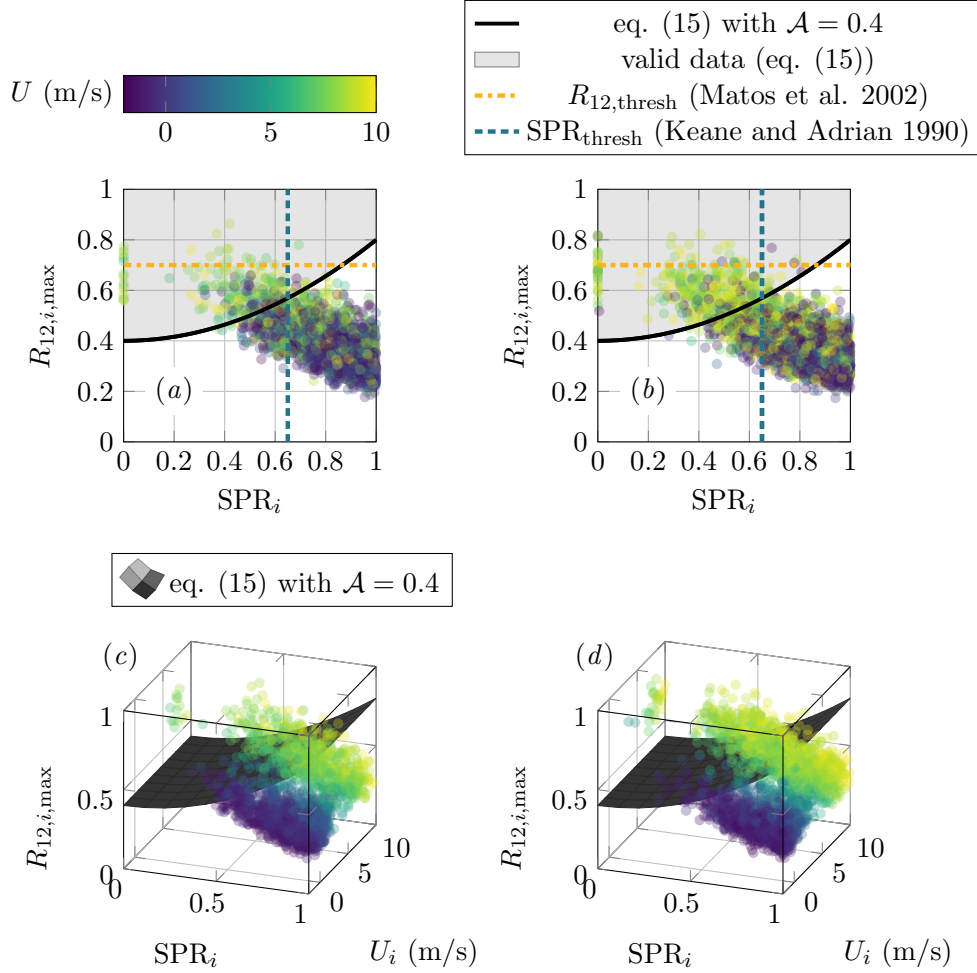


Figure 4: Instantaneous  $U_i$ ,  $R_{12,i,\max}$  and  $\text{SPR}_i$  for two measurement locations next to the bottom of the tunnel chute, processed with  $N_p = 6$  (a)  $R_{12,i,\max}$  versus  $\text{SPR}_i$  at  $y = 4.5$  mm (b)  $R_{12,i,\max}$  versus  $\text{SPR}_i$  at  $y = 10.5$  mm (c)  $R_{12,i,\max}$  versus  $\text{SPR}_i$  versus  $U_i$  at  $y = 4.5$  mm (d)  $R_{12,i,\max}$  versus  $\text{SPR}_i$  versus  $U_i$  at  $y = 10.5$  mm.

#### 4.1.2. Number of particles $N_p$

The duration of the adaptive windows is linked to the number of particles in the windows for the leading and trailing tips (figure 1b). A large window duration can lead to a smoothing/averaging of the velocity fluctuations and therefore to an underestimation of the turbulence levels (Kramer et al., 2019). A more accurate estimation of the pseudo-instantaneous interfacial velocity is

therefore expected with smaller window sizes, hence smaller  $N_p$ . However, a smaller number of particles  $N_p$  may lead to non-physical velocity estimations.

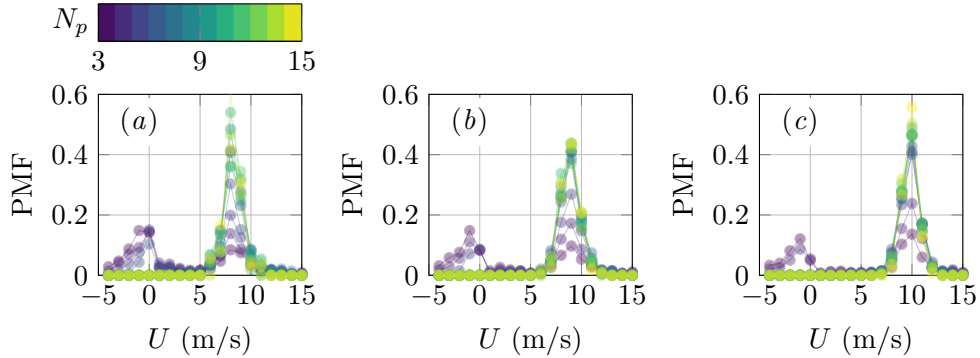


Figure 5: Unimodal and (non-physical) bimodal velocity distributions for different number of particles  $N_p$  in a high-speed air-water flow down a tunnel chute close to bottom level, processed with  $\mathcal{A} = 0.4$  (a)  $y = 4.5$  mm;  $C = 0.028$ ;  $F = 362$  s<sup>1</sup>/s (b)  $y = 10.5$  mm;  $C = 0.045$ ;  $F = 493$  s<sup>-1</sup> (c)  $y = 20.5$  mm;  $C = 0.066$ ;  $F = 638$  s<sup>-1</sup>.

In turbulent air-water flows, three-dimensional motion increases the probability that particles are detected only by one tip. In very small windows, random solitary interfaces weight considerably, sometimes resulting in velocity PMFs around zero, which is a non-physical estimation (figures 4, 5). This behaviour was observed in regions with high turbulence intensities, e.g. close to a solid boundary. The window duration, and therefore  $N_p$ , must be large enough to ensure that a single interfacial event cannot impair the velocity estimation. Using eq. (15) with  $\mathcal{A} = 0.4$ , a number of particles  $5 \leq N_p \leq 15$  was found appropriate to eliminate non-physical velocities close to zero (figure 5).

#### 4.2. Boundary layer flows: ETH tunnel chute and EPFL stepped spillway

The phase-detection probe datasets of the smooth tunnel chute (CP and FO) and the stepped spillway (CP) were processed with the AWCC technique following section 2. The number of particles was varied between  $5 \leq N_p \leq 15$  and  $\mathcal{A} = 0.4$  was used for cross-correlation based filtering (eq. (15)). Similar to Straub and Anderson (1958) and Zhang (2017), vertical coordinates were normalised with  $Y_{50}$ , i.e. the elevation where  $C = 0.5$ .

#### 4.2.1. Mean velocity and velocity fluctuations

Mean velocities  $\langle U \rangle$  obtained with the AWCC were in close agreement with those of the conventional cross-correlation technique for the re-analysed datasets (figures 6a,d and 7a).

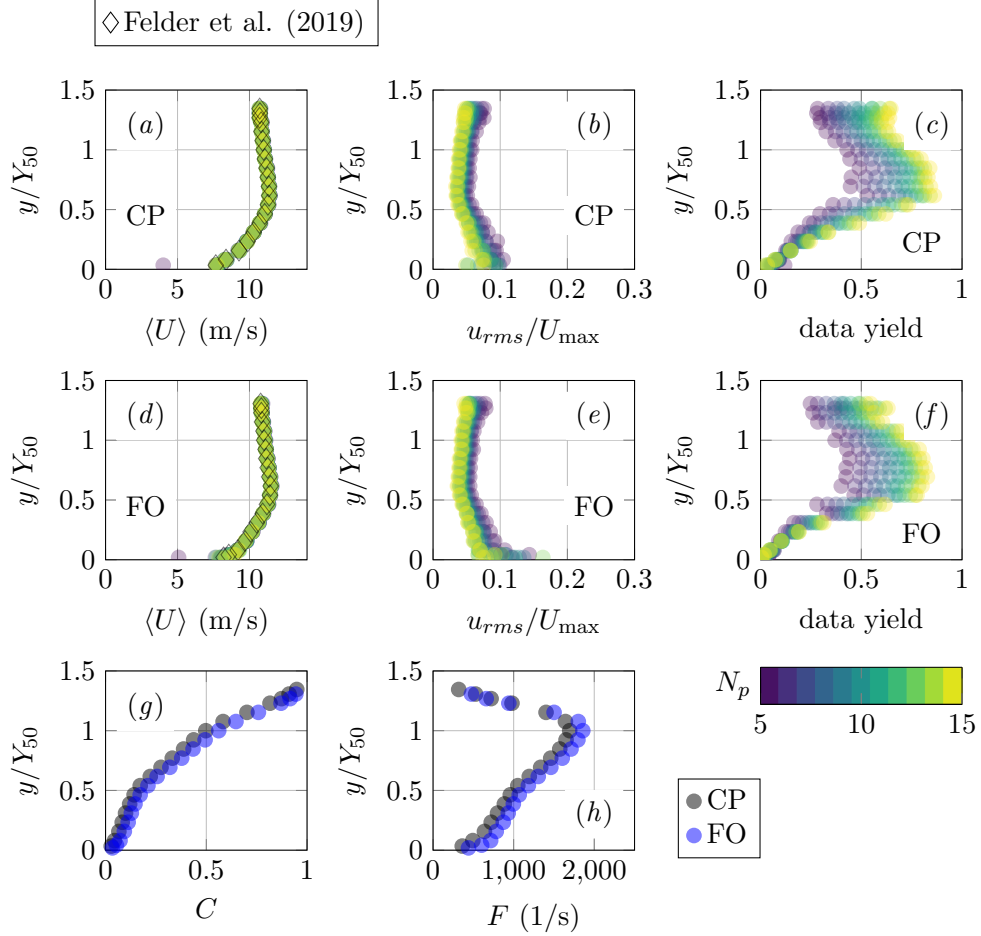


Figure 6: Tunnel chute: application of the AWCC technique with different  $N_p$  and  $\mathcal{A} = 0.4$ ; conductivity probe (CP) versus fiber optical (FO) probe (a) CP: mean velocities (b) CP: turbulent fluctuations (c) CP: data yield (d) FO: mean velocities (e) FO: turbulent fluctuations (f) FO: data yield (g) void fraction (h) particle count rate.

As shown in Kramer et al. (2019), the estimated mean velocities were independent of the number of particles  $N_p$ . The velocity profile in the tunnel chute showed a velocity-dip, typical for small aspect ratios (Hohermuth,

2019), whereas the profile on the stepped spillway followed closely a power law (Chanson, 2013). The scatter in  $\langle U \rangle$  close to the bed of both chutes was due to low data rates and is anticipated to disappear with longer sampling durations. For the tunnel chute, the mean velocity profiles measured with the conductivity probe (CP) and the fibre-optical probe (FO) were similar (figures 6*a,d*). However, the FO probe resulted in slightly larger velocities close to the chute bottom, which is expected to be related to the smaller probe tips (Vejrazka et al., 2010).

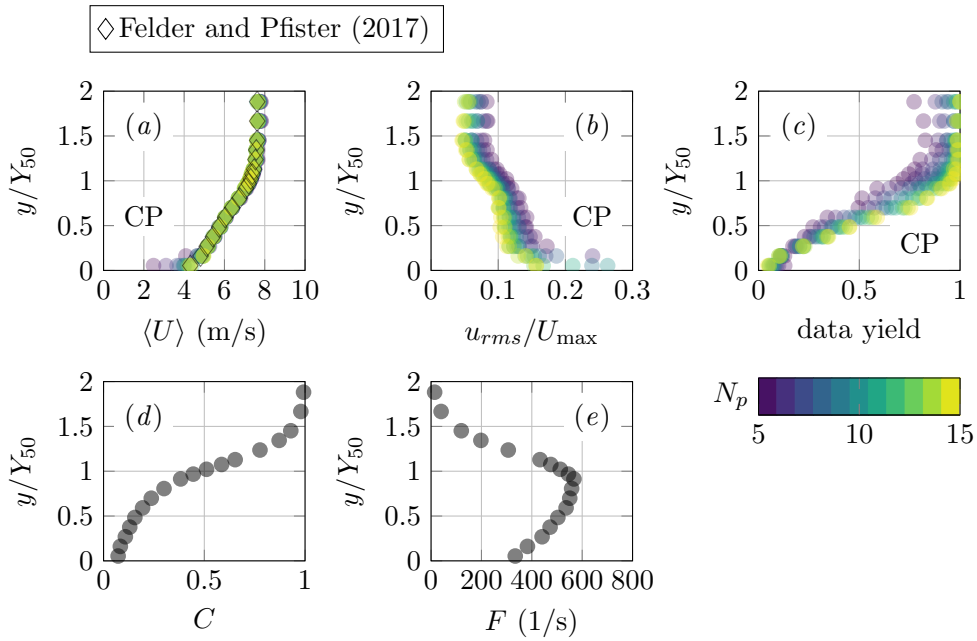


Figure 7: Stepped spillway: application of the AWCC technique with different  $N_p$  and  $\mathcal{A} = 0.4$ ; measurements undertaken with conductivity probe (CP) (a) mean velocities (b) turbulent fluctuations (c) data yield (d) void fraction (e) particle count rate.

Turbulent fluctuations were evaluated on the basis of eq. (14), normalised with the maximum cross-sectional velocity  $U_{max}$  (figures 6*b,e* and 7*b*). High fluctuations were found next to the bed of the tunnel chute and close to the pseudo-bottom of the stepped spillway. The streamwise normal Reynolds stresses were similar to boundary layer flows (Pope, 2000), albeit with slightly larger turbulence levels in air-water flows. The velocity fluctuations were higher on the stepped spillway compared to the tunnel chute due to the macro-roughness of the steps, showing a small bump at lower depths.

The scatter for  $5 \leq N_p \leq 6$  was due to the bimodal velocity distributions observed for small  $N_p$  (see figure 5), whereas the decrease in turbulence levels for  $N_p \geq 7$  was due to averaging effects with increasing window duration (Appendix B). There was no significant difference in measured turbulence intensities for CP and FO probes, confirming that the AWCC is applicable to different types of phase-detection probes.

The data yield was approximately  $0.05 < \text{data yield} < 0.95$  (figures 6c,f and 7c) and increased with distance from the bottom, which was directly related to the distribution of void fractions and particle count rates (figures 6g,h and 7d,e), combined with greater probabilities of single-tip impacts in flow regions with high turbulence intensities.

#### 4.2.2. Time-resolving turbulent properties: a word of caution

The calculation of pseudo-instantaneous interfacial velocities with the AWCC technique may allow to uncover further turbulence properties. Figure 8a shows pseudo-instantaneous velocity time series for different number of particles, recorded at a distance of  $y = 100.5$  mm from the bed of the tunnel chute. As discussed in section 4.1.2, increasing  $N_p$  resulted in a smoothing of the velocity time series.

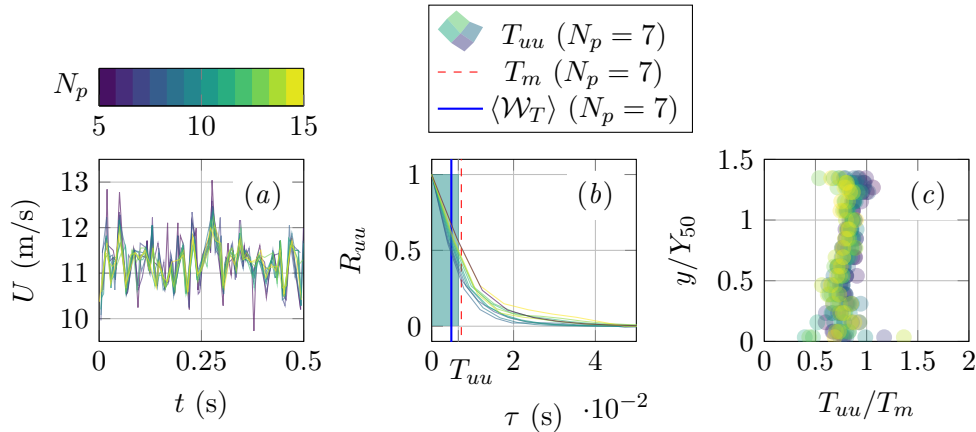


Figure 8: Time-resolving turbulent properties (tunnel chute) for different  $N_p$ , recorded with a conductivity probe (CP) (a) pseudo-instantaneous velocity time series at  $y = 100.5$  mm (only 0.5 s are shown for clarity) (b) ACFs, integral time scale ( $T_{uu}$ ), measurement time scale ( $T_m$ ) and mean window duration ( $\langle W_T \rangle$ ) at  $y = 100.5$  mm (c) data density ( $T_{uu}/T_m$ ) across the air-water column.

Auto-correlation functions (ACF) for different numbers of particles were

calculated using NN-resampling and ARMA model fitting (section 2.4) (figure 8b). The ACFs demonstrated a subtle trend of increasing auto-correlation coefficient ( $R_{uu}$ ) with increasing  $N_p$ , which might be due to the stronger influence of resampling at lower data rates or larger  $N_p$ , respectively. The integral velocity time scale ( $T_{uu}$ ) represents a measure of the *memory* of the flow (Kundu et al., 2016) and was calculated by integrating the ACF to the first zero-crossing:

$$T_{uu} = \int_{\tau=0}^{\tau(R_{uu}=0)} R_{uu}(\tau) d\tau \quad (16)$$

with  $\tau$  the lag time. As shown in figure 8b, the integral time scale  $T_{uu}$  is equal to the area under a rectangle of unity height. The measurement time scale  $T_m = 1/f_m$  is defined as the reciprocal of the mean data rate (figure 8b). To avoid velocity bias and aliasing, a data density (= ratio of the integral time scale to the measurement time scale) in the order of  $T_{uu}/T_m > 5$  (Winter et al., 1991) or  $T_{uu}/T_m > 10$  (Damaschke et al., 2018) is typically recommended.

In this study, it was observed that  $T_{uu}/T_m$  was slightly below unity across the full air-water flow column of the tunnel chute (figure 8c). This finding implies that the AWCC data density did not allow for a reliable quantification of time-resolving turbulent properties. For  $N_p = 7$ , even a 100 % data yield would be insufficient for an unbiased estimation of  $T_{uu}$ , i.e.  $T_{uu}/\langle W_T \rangle < 10$  (figure 8b). Moving towards single event detection techniques or improving the design of the probes may help to overcome these limitations in the future.

#### 4.3. Shear layer flow: the UNSW hydraulic jump

The hydraulic jump is a well-known hydraulic phenomena that constitutes a transition from supercritical to subcritical flow conditions. The measured void fraction and particle count rate distributions showed typical profiles with two peaks (figures 9d,e), one in the shear layer and one in the recirculation region (Murzyn et al., 2005; Wang and Chanson, 2015; Montano, 2019).

Due to the complex nature of fully aerated hydraulic jumps, the measurement of interfacial velocities is challenging and limitations exist in the upper flow region, which is due to three-dimensional velocity contributions. Herein, the AWCC was applied to provide mean interfacial velocities and turbulence levels. Next to the channel bed, the interfacial velocity distribution was similar to a wall-jet (Rajaratnam, 1965). Largest velocities were observed for the impinging jet, followed by a shear layer and on average negative velocities in the recirculation region (figure 9a). A continuous velocity profile was

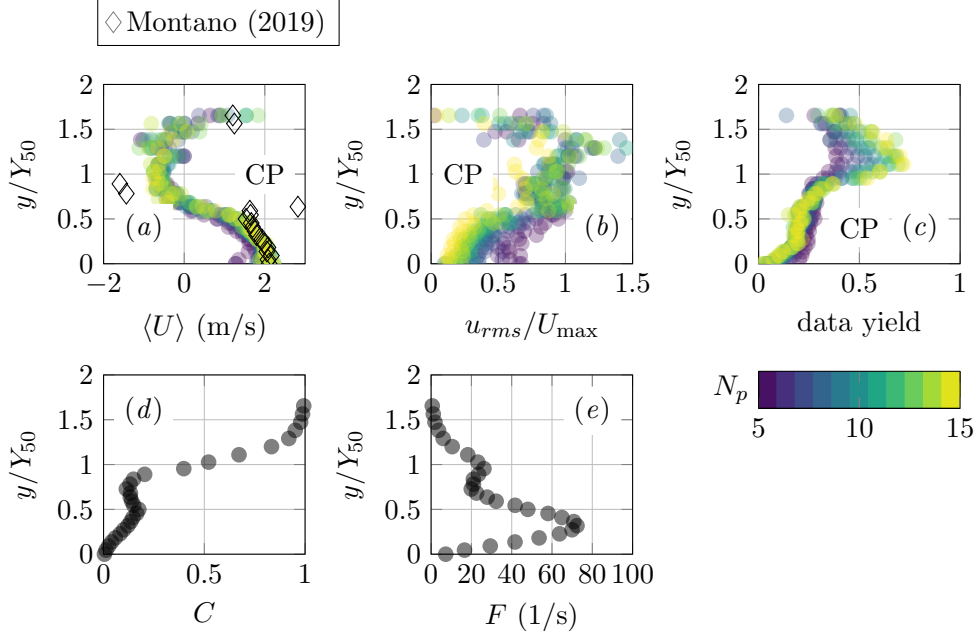


Figure 9: Hydraulic jump: application of the AWCC technique with different  $N_p$  and  $\mathcal{A} = 0.4$ ; measurements undertaken with a conductivity probe (CP) (a) mean velocities (b) turbulent fluctuations (c) data yield (d) void fraction (e) particle count rate.

attained irrespective of  $N_p$ , which resembled the results presented by Zhang et al. (2014) and Kramer and Valero (2019b).

The turbulence levels indicated significant turbulent interfacial interactions with largest levels within the recirculation region (figure 9b). It must be noted that a misalignment of the probe tips with flow streamlines, especially in the recirculation region, and high turbulence levels may have led to an increase of the measurement uncertainty (see also table 2). Despite a data yield  $< 0.7$  over the whole water column (and below 0.3 for  $y < 80$  mm), the shape of interfacial velocity and turbulence intensity distributions remained continuous for a sampling duration of  $T = 300$  s.

## 5. Discussion

### 5.1. Comparison to conventional processing techniques

The AWCC technique (Kramer et al., 2019) with present modifications offers an alternative to conventional methods described in section 1.1. With

the conventional method, interfacial mean velocities are typically evaluated from cross-correlation analysis of the complete raw signal (Toombes, 2002) or from an ensemble-averaged analysis of sub-segments with a sub-sample duration between 3 to 5 s (Felder and Chanson, 2015). Conventional turbulence level estimations are based on eq. (2), proposed by Chanson and Toombes (2002).

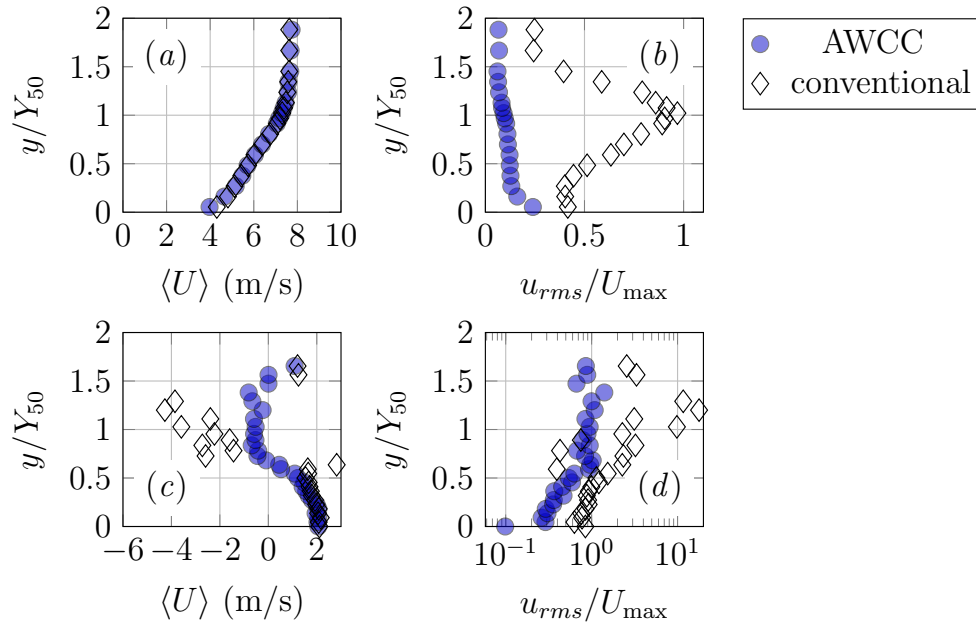


Figure 10: Comparison of the AWCC technique ( $N_p = 10$  and  $\mathcal{A} = 0.4$ ) with conventional signal processing after Chanson and Toombes (2002); measurements undertaken with conductivity probes (CP) (a) stepped spillway: mean velocity profiles (b) stepped spillway: streamwise turbulent fluctuations (c) hydraulic jump: mean velocity profiles (d) hydraulic jump: streamwise turbulent fluctuations.

In high-velocity air-water flows down stepped and smooth chutes with a clearly defined main flow direction, the mean flow velocities estimated with the AWCC technique and the conventional approach were in close agreement (figure 10a). However, the conventional mean velocity estimation is based on the analysis of a *single* ensemble-averaged cross-correlation function, which does not allow for the detection of fluctuating signs and near-null velocities (as discussed by Wang and Chanson, 2015). In shear layer flows, the conventional processing therefore resulted in a non-physical overestimation of the recirculation velocity (figure 10c). The AWCC allowed the consistent

characterisation of the jump’s shear layer and the results were similar to observations of a jump with  $Fr_1 = 5.43$  (Zhang et al., 2014). Note that the AWCC results were further validated via image-based velocimetry from a sidewall perspective by Kramer and Valero (2019b).

Streamwise turbulence levels computed with the conventional approach were significantly larger than the AWCC results (figure 10*b*). While the AWCC data followed a profile similar to a single-phase flow with maximum turbulence intensities close to the pseudo-bottom (as demonstrated in Amador et al., 2006), the method of Chanson and Toombes (2002) resulted in a local maximum in the intermediate flow region at  $y \approx 100$  mm (figure 10*b*). This overestimation is a result of the shortcomings of eq. (2) as discussed in section 1.1. Unrealistically high turbulence levels of  $u_{rms}/U_{max} \approx 18$  (figure 10*d*) were also observed with the conventional method for shear layer flows in the hydraulic jump (see also Zhang et al., 2014). In contrast, the AWCC technique provided continuous profiles of much lower turbulence levels.

Based on the observations made herein, the conventional method should only be applied to calculate mean streamwise velocities in air-water flows with mostly unidirectional flow velocity (i.e. spillways and chutes), while conventional turbulence levels must be treated with caution for any type of air-water flow. The AWCC provides a more consistent estimation of near-null velocities and turbulent fluctuations, but is also not completely free of biases; e.g. particle-probe interaction and a variation of the angle of attack are believed to increase the measurement uncertainty (Thorwarth, 2008; Vejrazka et al., 2010). The use of synthetic signals and the comparison to other, preferably non-intrusive, measurements techniques can help to refine the technique in future works.

### *5.2. Overcoming the window-smoothing effect: extrapolation of turbulence levels to $N_p = 1$*

To overcome the practical limitation of processing with a very small number of particles, the convergence of velocity fluctuations for single particles ( $N_p = 1$ ) was investigated for the chute datasets. Figure 11 depicts measured turbulence intensities versus  $N_p$ . Data points with very low or very high void fractions, e.g. close to the bed of the chutes or in the upper flow region, were excluded from the analysis due to potentially non-physical velocities and insufficient data rates. Estimated fluctuations decreased with increasing  $N_p$

and followed an expression derived using stochastic signals (Appendix B):

$$u_{rms}/u_{rms,max} = 1 - \mathcal{K}_1 \ln(N_p)^{\mathcal{K}_2} \quad \{N_p \in \mathbb{Z}^+ : 1 \leq N_p \leq 100\} \quad (17)$$

where  $u_{rms,max}$  is a parameter that represents the extrapolated root mean square of velocity fluctuations for  $N_p = 1$  at each depth  $y$ . The equation was valid up to  $N_p \approx 100$  and the constants took the values  $\mathcal{K}_1 = 0.07$  and  $\mathcal{K}_2 = 1.55$  for the available data (figure 11).

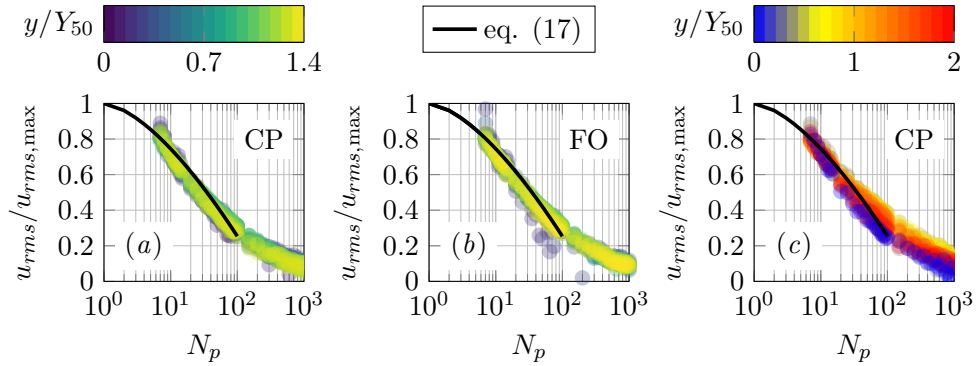


Figure 11: Normalised turbulent fluctuations ( $u_{rms}/u_{rms,max}$ ) versus  $N_p$  for the tunnel chute and the stepped spillway, processed with  $\mathcal{A} = 0.4$  (a) conductivity probe (CP) measurements of the tunnel chute (b) fiber optical probe (FO) measurements of the tunnel chute (c) conductivity probe (CP) measurements of the stepped spillway.

Independent of the type of phase-detection probe, eq. (17) showed good agreement for different types of air-water flows. The obtained values imply that velocity fluctuations for  $N_p = 10$  are roughly 70 % of those ideally expected for  $N_p = 1$ , and 30 % for  $N_p = 100$ . It is stressed that the constants  $\mathcal{K}$  are a function of the particle count rate  $F$ , the turbulence level  $Tu$  and the integral time scale  $T_{uu}$  of the flow. Therefore, it is recommended to perform a calibration before extrapolating turbulence levels with eq. (17).

### 5.3. Best practices for the AWCC technique

While the AWCC technique cannot solve all limitations of phase-detection probes, it helps alleviating shortcomings of conventional analysis methods. The sensitivity analysis of the AWCC technique for three different flow types revealed that the optimum processing parameters are in the same range for all tested flow conditions and probe types (side-by-side tip design). Best practice recommendations for the AWCC technique are as follows:

1. Select an appropriate cross-correlation based filtering approach, starting with eq. (15) using  $\mathcal{A} = 0.4$ .
2. Select the number of particles  $N_p$  within a recommended range between  $5 \leq N_p \leq 15$ . It is advised to perform a sensitivity analysis similar to figure 5, with the aim to keep  $N_p$  small while avoiding non-physical velocity information (i.e. bimodal PMF).
3. Correct the velocity bias using a suitable weighting scheme (equations (13) and (14)). Window duration weighting and interarrival time weighting showed a similar performance, whereas inverse absolute velocity weighting led to unreasonable mean velocities in free-shear regions characterised by near-zero velocities.
4. When the focus is on turbulence quantities, eq. (17) can be used to extrapolate turbulence intensities to  $N_p = 1$ . Because the constants  $\mathcal{K}$  may be a function of sampling parameters and flow properties, a calibration is necessary.
5. A sufficient number of valid pseudo-instantaneous velocity data must be recorded to reduce the uncertainty in the estimation of mean and turbulent properties (Appendix A). A low data yield directly implies the need for longer sampling durations. In such cases, it is recommended to increase the sampling duration until the moments of the velocity samples converge.

## 6. Conclusion

This study presented a detailed sensitivity analysis of the adaptive window cross-correlation (AWCC) technique for processing dual-tip phase-detection probe signals in highly-aerated flows. The re-analysed experimental datasets covered three common air-water flow phenomena, including a smooth tunnel chute, a stepped spillway and a hydraulic jump.

It was observed that a cross-correlation based filtering approach performed well for all flow conditions, regardless of the deployed dual-tip phase-detection probe (fiber optical and conductivity probe) with side-by-side tip design. Mean velocities were independent of the number of particles ( $N_p$ ) per window, but estimated velocity fluctuations decreased with increasing  $N_p$ . Stochastic signals were used to derive an empirical expression that allows the extrapolation of turbulence levels to  $N_p = 1$ , thereby solving the practical limitation that recorded signals cannot be processed with very small numbers of particles.

A comparison with conventional signal processing confirmed that these methods were not able to measure near-null velocities, as those in the shear layer of hydraulic jumps. As mentioned in Zhang et al. (2014), the computation of turbulence levels from standard deviations of auto- and cross-correlation functions (of the raw voltage signals) seemed to significantly overestimate the turbulence intensity and published data must be treated with caution.

The AWCC technique allows a reliable analysis of mean interfacial velocities and turbulent fluctuations in highly aerated flows. Its ability to uncover time-resolving turbulence statistics is currently limited by the data density. Future developments in terms of signal processing and optimized design of phase-detection probes may help to overcome these limitations. Best practices have been proposed to provide a clear guidance for future studies using the AWCC technique.

## Acknowledgements

The authors would like to thank Dr Laura Montano (WRL, UNSW Sydney) for providing the hydraulic jump data set and Rob Jenkins (WRL, UNSW Sydney) for manufacturing the WRL conductivity probes. We also would like to thank the anonymous reviewers for their valuable comments, which helped to improve the manuscript.

## Notation

$\mathcal{A}$	parameter for cross-correlation based filtering	(-)
$a$	constant	(-)
$b$	constant	(-)
$c(t)$	instantaneous void fraction (= binarized signal)	(-)
$C$	time-averaged void fraction	(-)
$d_c$	critical flow depth (stepped spillway)	(m)
$d_1$	inflow depth (hydraulic jump)	(m)
$e_{\langle U \rangle}$	relative error; $e_{\langle U \rangle} = (\langle U \rangle - \langle U \rangle_{\text{sim}}) / \langle U \rangle_{\text{sim}}$	(-)
$e_{Tu}$	relative error; $e_{Tu} = (Tu - Tu_{\text{sim}}) / Tu_{\text{sim}}$	(-)
$f$	sampling rate	(s <sup>-1</sup> )
$f_m$	data rate (valid windows per time)	(s <sup>-1</sup> )
$F$	time-averaged particle count rate	(s <sup>-1</sup> )
$Fr_1$	inflow Froude number (hydraulic jump)	(-)

$g$	gravitational acceleration	(m s <sup>-2</sup> )
$h_{\text{us}}$	flow depth upstream of sluice gate (tunnel chute)	(m)
$h$	step height (stepped spillway)	(m)
$h_g$	sluice gate opening (tunnel chute)	(m)
$H$	upstream head (tunnel chute)	(m)
$\mathcal{K}$	constants for extrapolating <i>rms</i> velocity fluctuations	(-)
$n_{\mathcal{W}}$	number of windows	(-)
$m_a$	mode representing the air phase	(V)
$m_w$	mode representing the water phase	(V)
$N$	number of detected particles	(-)
$N_e$	ensemble size	(-)
$N_p$	selected number of particles to determine window sizes	(-)
$q$	specific water discharge	(m <sup>2</sup> s <sup>-1</sup> )
$Re$	Reynolds number	(-)
$R_{uu}$	auto-correlation coefficient	(-)
$R_{12}$	cross-correlation coefficient	(-)
$R_{12,\text{thresh}}$	threshold for the cross-correlation coefficient	(-)
$S(\mathbf{x}, t)$	raw phase-detection probe signal	(V)
SPR	secondary peak ratio	(-)
SPR <sub>thresh</sub>	threshold for the secondary peak ratio	(-)
$T$	sampling duration	(s)
$T_m$	measurement time scale, $T_m = 1/f_m$	(s)
$T_{wu}$	integral velocity time scale	(s)
$\mathcal{T}_i$	interfacial travel time	(s)
$Tu$	turbulence intensity, defined as $Tu = u_{rms}/\langle U \rangle$	(-)
$t$	time	(s)
$t_{ch,a}$	air chord time	(s)
$t_{ch,w}$	water chord time	(s)
$t_{s,i}$	start time of window $i$	(s)
$t_{e,i}$	end time of window $i$	(s)
$U$	instantaneous streamwise velocity	(m s <sup>-1</sup> )
$\langle U \rangle$	time-averaged streamwise velocity	(m s <sup>-1</sup> )
$U_{\text{max}}$	maximum time-averaged cross-sectional velocity	(m s <sup>-1</sup> )
$u$	fluctuating part of the streamwise velocity	(m s <sup>-1</sup> )
$\mathcal{W}_T$	window duration	(s)
$w$	weighting factor for velocity bias correction	(-)
$x$	streamwise coordinate	(m)
$\mathbf{x}$	coordinate vector	

$Y_{50}$	vertical elevation where $C = 0.5$	(m)
$y$	vertical coordinate	(m)

#### Greek letters

$\Delta x$	streamwise tip separation	(m)
$\nu$	kinematic viscosity of water	(m <sup>2</sup> /s)
$\sigma$	standard deviation	(s)
$\tau$	time lag of the auto- or cross-correlation function	(s)
$\phi$	diameter	(mm)

#### Abbreviations, operators and subscripts

$\langle \dots \rangle$	time-average over measurement time $T$
$[\cdot]$	floor function
1, 2	leading and trailing tip
ACF	autocorrelation function
ARMA	autoregressive moving-average model
AWCC	adaptive window cross correlation
CP	phase-detection conductivity probe
FO	phase-detection fiber optical probe
$i$	running variable
$j$	running variable
LDA	laser Doppler anemometer
max	maximum
NN	nearest-neighbor resampling
PIV	particle image velocimetry
PMF	probability mass function
PSD	power spectral density function
$rms$	square root of mean velocity fluctuations
ROC	robust outlier cutoff
sim	simulation

#### References

- Amador, A., Sánchez-Juny, M., Dolz, J., 2006. Characterization of the Non-aerated Flow Region in a Stepped Spillway by PIV. *Journal of Fluids Engineering* 128, 1266–1273.

- Andre, S., Boillat, J.L., Schleiss, A., 2005. Discussion of Two-phase flow characteristics of stepped spillways by Robert M. Boes and Willi H. Hager. *Journal of Hydraulic Engineering* 131, 423–427.
- Barrau, E., Riviere, N., Poupot, C., Cartellier, A., 1999. Single and double optical probes in air-water two-phase flows: real time signal processing and sensor performance. *International Journal of Multiphase Flow* 25, 229–256.
- Benedict, L., Nobach, H., Tropea, C., 2000. Estimation of turbulent velocity spectra from laser doppler data. *Measurement Science and Technology* 11, 1089–1104.
- Boes, R.M., 2000. Zweiphasenströmung und Energieumsetzung an Grosskaskaden. Ph.D. thesis. ETH Zurich.
- Britz, D., Antonia, R., 1996. A comparison of methods of computing power spectra of LDA signals. *Measurement Science and Technology* 7, 1042–1053.
- Brocchini, M., Peregrine, D.H., 2001. The dynamics of strong turbulence at free surfaces. part 1. description. *Journal of Fluid Mechanics* 449, 225–254.
- Broersen, P., de Waale, S., Bos, R., 2000. The accuracy of time series analysis for laser Doppler velocimetry, in: 10th International Symposium on Application of Laser Technology to Fluid Mechanics, Lisbon.
- Buchhave, P., George, W.K., Lumley, J.L., 1979. The measurement of turbulence with the laser-doppler anemometer. *Annual Review of Fluid Mechanics* 11, 443–503.
- Cain, P., Wood, I.R., 1981. Instrumentation for aerated flow on spillways. *Journal of the Hydraulics Division* 107, 1407–1424.
- Cartellier, A., 1992. Simultaneous void fraction measurement, bubble velocity, and size estimate using a single optical probe in gasliquid two-phase flows. *Review of Scientific Instruments* 63, 5442–5453.
- Cartellier, A., 1998. Measurement of gas phase characteristics using new monofiber optical probes and real-time signal processing. *Nuclear Engineering and Design* 184, 393–408.

- Cartellier, A., 2006. Optical probes for multiphase flows. *Encyclopedia of sensors* 7, 239–258.
- Cartellier, A., Achard, J., 1991. Local phase detection probes in fluid/fluid two-phase flows. *Review of Scientific Instruments* 62, 279–303.
- Chang, K.A., Lim, H.J., Chin, B.S., 2003. Fiber optic reflectometer for velocity and fraction ratio measurements in multiphase flows. *Review of Scientific Instruments* 74, 3559–3564.
- Chanson, H., 2002. Air-water flow measurements with intrusive, phase-detection probes: can we improve their interpretation? *Journal of Hydraulic Engineering* 128, 252–255.
- Chanson, H., 2013. Hydraulics of aerated flows: qui pro quo? *Journal of Hydraulic Research* 51, 223–243.
- Chanson, H., 2016. Phase-detection measurements in free-surface turbulent shear flows. *Journal of Geophysics and Engineering* 13, 74–87.
- Chanson, H., Toombes, L., 2002. Air–water flows down stepped chutes: turbulence and flow structure observations. *International Journal of Multiphase Flow* 28, 1737–1761.
- Crowe, C.T., Schwarzkopf, J.D., Sommerfeld, M., Tsuji, Y., 2011. *Multiphase Flows with Droplets and Particles*. 2 ed., CRC Press.
- Cummings, P.D., Chanson, H., 1997. Air entrainment in the developing flow region of plunging jets part 2: Experimental. *Journal of Fluids Engineering* 119, 603–608.
- Damaschke, N., Khn, V., H., N., 2018. A fair review of non-parametric bias-free autocorrelation and spectral methods for randomly sampled data in laser doppler velocimetry. *Digital Signal Processing* 76, 22–33.
- Felder, S., Chanson, H., 2015. Phase-detection probe measurements in high-velocity free-surface flows including a discussion of key sampling parameters. *Experimental and Thermal Fluid Science* 61, 66–79.
- Felder, S., Hohermuth, B., Boes, R.M., 2019. High-velocity air-water flows downstream of sluice gates including selection of optimum phase-detection probe. *International Journal of Multiphase Flow* 116, 203–220.

- Felder, S., Pfister, M., 2017. Comparative analyses of phase-detective intrusive probes in high-velocity airwater flows. *International Journal of Multiphase Flow* 90, 88–101.
- Goring, D.G., Nikora, V.I., 2002. Despiking Acoustic Doppler Velocimeter Data. *Journal of Hydraulic Engineering* 128, 117–126.
- Hain, R., Kaehler, C.J., 2007. Fundamentals of multiframe particle image velocimetry (PIV). *Experiments in Fluids* 42, 575–578.
- Herringe, R.A., Davis, M.R., 1976. Structural development of gas-liquid mixture flows. *Journal of Fluid Mechanics* 73, 97–123.
- Hoesel, W., Rodi, W., 1977. New biasing elimination method for laser Doppler velocimeter counter processing. *Review of Scientific Instruments* 48, 910–919.
- Hohermuth, B., 2019. Aeration and two-phase flow characteristics of low-level outlets. Ph.D. thesis. ETH Zurich, Switzerland. doi: <https://doi.org/10.3929/ethz-b-000351715>.
- Jones, O.C., Delhaye, J.M., 1976. Transient and statistical measurement techniques for twophase flows: a critical review. *International Journal of Multiphase Flow* 3, 89–116.
- Kataoka, I., Ishii, M., Serizawa, A., 1986. Local formulation and measurements of interfacial area concentration in two-phase flow. *International Journal of Multiphase Flow* 12, 505–529.
- Keane, R.D., Adrian, R.J., 1990. Optimization of particle image velocimeters. I. Double pulsed systems. *Measurement Science and Technology* 1, 1202–1205.
- Kiambi, S.L., Duquenne, A.M., Dupont, J.B., Colin, C., Risso, F., Delmas, H., 2003. Measurements of bubble characteristics: Comparison between double optical probe and imaging. *The Canadian Journal of Chemical Engineering* 81, 764–770.
- Kramer, M., 2019. Particle size distributions in turbulent air water flows, in: *E-Proceedings of the 38th IAHR World Congress, Panama City, Panama*. pp. 5722–5731.

- Kramer, M., Valero, D., 2019a. Phase-detection signal processing toolbox. Github repository. doi: <http://dx.doi.org/10.5281/zenodo.2542958>.
- Kramer, M., Valero, D., 2019b. Turbulence and self-similarity in highly aerated shear flows: the stable hydraulic jump. arXiv:1907.04989v1 .
- Kramer, M., Valero, D., Chanson, H., Bung, D.B., 2019. Towards reliable turbulence estimations with phase-detection probes: an adaptive window cross-correlation technique. *Experiments in Fluids* 60:2, 6 pages.
- Kundu, P.K., Cohen, I.M., Dowling, D.R., 2016. *Fluid Mechanics*. 6 ed., Academic Press.
- Langevin, P., 1908. Sur la thorie du mouvement brownien. *Comptes-rendus de l'Academie des sciences Paris* 146, 530–533.
- Matos, J., Frizell, K.H., Andre, S., Frizell, K.W., 2002. On the performance of velocity measurement techniques in air-water flows, in: *Proceedings of the EWRI/IAHR joint conference on hydraulic measurements & experimental methods* ASCE, Estes Park, USA.
- McLaughlin, D.K., Tiederman, W.G., 1973. Biasing correction for individual realization of laser anemometer measurements in turbulent flows. *Physics of Fluids* 16, 2082–2088.
- Montano, L., 2019. An experimental study of free-surface dynamics and internal motions in fully aerated hydraulic jumps. Ph.D. thesis. UNSW Sydney, Australia.
- Murzyn, F., Mouazé, D., Chaplin, J.R., 2005. Optical fibre probe measurements of bubbly flow in hydraulic jumps. *International Journal of Multiphase Flow* 31, 141–154.
- Neal, L.G., Bankoff, S.G., 1963. A High Resolution Resistivity Probe for Determination of Local Void Properties in Gas-Liquid Flow. *AICHE Journal* 9, 490–494.
- Pope, S.B., 2000. *Turbulent Flows*. Cambridge University Press.
- Rajaratnam, N., 1965. The hydraulic jump as wall jet. *Journal of the Hydraulics Division* 91, 107–132.

- Revankar, S.T., Ishii, M., 1993. Theory and measurement of local interfacial area using a four sensor probe in two-phase flow. *International Journal of Heat and Mass Transfer* 36, 2997–3007.
- Sene, K.J., 1984. Aspects of bubbly two-phase flow. Ph.D. thesis. University of Cambridge, U.K.
- Serdual, C.D., Loewen, M.R., 1998. Experiments investigating the use of fiber-optic probes for measuring bubble-size distributions. *IEEE Journal of Oceanic Engineering* 23, 385–399.
- Straub, L., Anderson, A., 1958. Experiments on self aerated flow in open channels. *Journal of the Hydraulics Division (ASCE)* 84(HY7), 1–35.
- Thorwarth, J., 2008. Hydraulics on Pooled Stepped Chutes - Self Induced Unsteady Flow and Energy Dissipation (in German). Ph.D. thesis. RWTH Aachen, Germany.
- Toombes, L., 2002. Experimental study of air-water flow properties on low-gradient stepped cascades. Ph.D. thesis. The University of Queensland, Australia.
- Valero, D., 2018. On the Fluid Mechanics of Self-Aeration in Open Channel Flows. Ph.D. thesis. Universite de Liege, Belgium; University of Applied Sciences Aachen, Germany.
- Valero, D., Bung, D.B., 2018a. Artificial neural networks and pattern recognition for air-water flow velocity estimation using a single-tip optical fibre probe. *Journal of Hydro-environment Research* 19, 150–159.
- Valero, D., Bung, D.B., 2018b. Reformulating self-aeration in hydraulic structures: Turbulent growth of free surface perturbations leading to air entrainment. *International Journal of Multiphase Flow* 100, 127–142.
- Valero, D., Kramer, M., Bung, D.B., Chanson, H., 2019. A stochastic bubble generator for air water flow research, in: *E-Proceedings of the 38th IAHR World Congress, Panama City, Panama*. pp. 5714–5721.
- Vejrazka, J., M, V., Orvalho, S., Sechet, P., Ruzicka, M.C., Cartellier, A., 2010. Measurement accuracy of a mono-fiber optical probe in a bubbly flow. *International Journal of Multiphase Flow* 36, 533–548.

- Velte, C.M., George, W.K., Buchhave, P., 2014. Estimation of burst-mode LDA power spectra. *Experiments in Fluids* 55, 1674.
- Wahl, T.L., 2003. Discussion of “Despiking Acoustic Doppler Velocimeter Data” by Derek G. Goring and Vladimir I. Nikora. *Journal of Hydraulic Engineering* 129, 484–487.
- Wang, F., Jin, N.D., Wang, D.Y., Han, Y.F., Liu, D.Y., 2017. Measurement of gas phase characteristics in bubbly oil-gas-water flows using bi-optical fiber and high-resolution conductance probes. *Experimental Thermal and Fluid Science* 88, 361–375.
- Wang, H., Chanson, H., 2015. Experimental study of turbulent fluctuations in hydraulic jumps. *Journal of Hydraulic Engineering* 141, 04015010.
- Van der Welle, R., 1985. Void fraction, bubble velocity and bubble size in two-phase flow. *International Journal of Multiphase Flow* 11, 317–345.
- Wilhelms, S.C., Gulliver, J.S., 2005. Bubbles and waves description of self-aerated spillway flow. *Journal of Hydraulic Research* 43, 522–531.
- Winter, A.R., Graham, L.J.W., Bremhorst, K., 1991. Velocity bias associated with laser doppler anemometer controlled processors. *Journal of Fluids Engineering* 113, 250–255.
- Zhang, G., 2017. Free-surface aeration, turbulence, and energy dissipation on stepped chutes with triangular steps, chamfered steps, and partially blocked step cavities. Ph.D. thesis. The University of Queensland, Brisbane.
- Zhang, W., Liu, M., Zhu, D., Rajaratnam, F., 2014. Mean and turbulent bubble velocities in free hydraulic jumps for small to intermediate froude numbers. *Journal of Hydraulic Engineering* 140, 04014055.

## **Appendix A. Convergence analysis - mean and turbulent properties**

The convergence analysis for mean void fraction  $C$ , mean flow velocity  $\langle U \rangle$  and root-mean-square velocity fluctuations  $u_{rms}$  was performed using the stepped spillway data. Running averages of  $C(N_e)$ ,  $\langle U(N_e) \rangle$ ,  $u_{rms}(N_e)$

were normalised with mean values  $C$ ,  $\langle U \rangle$ ,  $u_{rms}$  of the entire ensemble  $N_{e,max}$  (i.e.  $C(N_{e,max}) = C$ ) where  $N_e =$  ensemble size (figure A.12). The entire/maximum ensemble size for the computation of the void fraction was relatively large ( $N_{e,max} = f \cdot T = 2.25 \cdot 10^7$ , with  $f$  the sampling rate and  $T$  the sampling duration) and the best convergence was achieved in the upper flow region (figure A.12a), where turbulence quantities were the lowest. Slower convergence was observed close to chute invert and uncertainties of roughly  $\pm 2\%$  remained for the full sampling duration  $T = 45$  s.

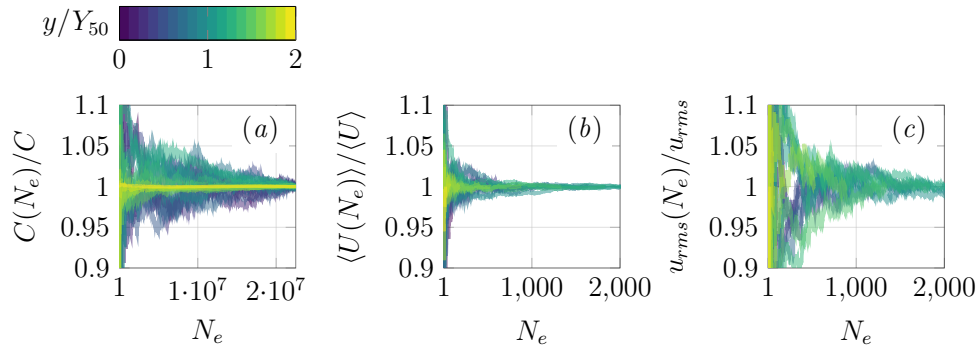


Figure A.12: Convergence analysis for mean and turbulent properties of the stepped spillway (a) mean void fraction (b) mean streamwise velocities, computed for  $N_p = 10$  (c) square root of mean velocity fluctuations, computed for  $N_p = 10$ .

The maximum ensemble sizes for the computation of mean velocities and velocity fluctuations were determined by the local particle count rate, the number of particles ( $N_p = 10$ ) and the local data yield ( $N_{e,max}(y) = n_W(y) \cdot \text{data.yield}(y)$ , with  $n_W$  the number of windows). Note that the maximum ensemble sizes (i.e. the maximum values on the abscissae for each curve in figure A.12) represent a sampling duration of  $T = 45$  s. Although  $n_W \cdot \text{data.yield} \ll f \cdot T$ , mean velocities converged relatively fast at around  $N_e \approx 1000$  irrespective of the measurement location (figure A.12b), whereas the convergence of the velocity fluctuations was slower compared to the mean velocities (figure A.12c). Overall, the largest ensemble size was required next to the chute invert due to the strongest turbulent fluctuations and three-dimensional motions within this flow region. A sampling duration  $T > 45$  s is necessary to achieve convergence uncertainties below  $\approx \pm 2\%$ .

## Appendix B. Extrapolation of turbulence levels - stochastic approach

The extrapolation of velocity fluctuations to single particles ( $N_p = 1$ ) was derived using stochastic modelling. Turbulent velocity time series were generated using the Langevin equation (Langevin, 1908), governing a stochastic process  $u^*$  with mean zero and integral time-scale  $T_{uu}$  (Pope, 2000):

$$u^*(t + \delta t) = u^*(t) \left(1 - \frac{\delta t}{T_{uu}}\right) + u_{rms}^* \left(\frac{2 \delta t}{T_{uu}}\right)^{1/2} \xi(t) \quad (\text{B.1})$$

for time steps  $\delta t \ll T_{uu}$ , where  $\xi(t)$  is a standardized Gaussian random variable. The modelled velocity  $u^*$  represents the fluctuating particle velocity  $u$  and was superimposed to a time-averaged velocity  $\langle U \rangle$ .

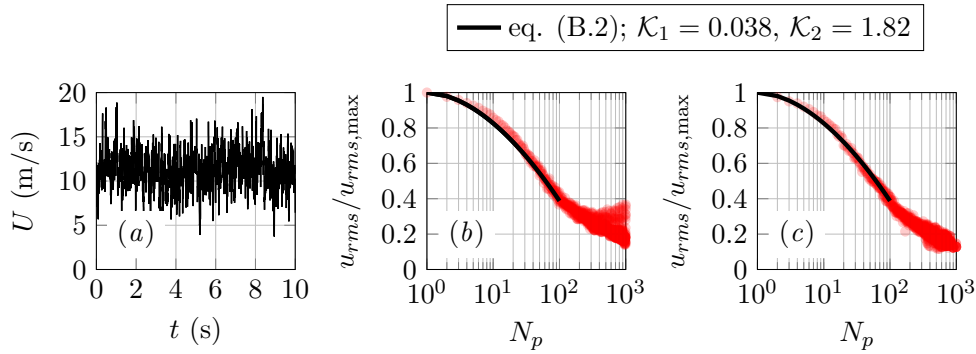


Figure B.13: Stochastic extrapolation of turbulent velocity fluctuations *a*) time series of stochastic velocities  $U$ , generated using eq. (B.1) and  $\langle U \rangle = 11$  m/s,  $Tu = 0.2$ ,  $T_{uu} = 0.05$  s,  $T = 45$  s (only 10 s shown for clarity) and  $f = 200$  1/s *b*) normalised *rms* fluctuations evaluated using different number of particles/measurement points from the stochastic signals shown on the left *c*) normalised *rms* fluctuations for virtual phase-detection probe data from Kramer et al. (2019) with  $\langle U \rangle = 2.99$  m/s,  $Tu = 0.2$ ,  $T_{uu} = 0.06$  s,  $C = 0.7$ ,  $F = 140$  and  $T = 90$  s.

The signal was sampled at  $f = 200$  Hz for  $\langle U \rangle = 11$  m/s,  $Tu = 0.2$  and  $T_{uu} = 0.05$  s. The sampling duration was  $T = 45$  s and the root mean square of the velocity fluctuations was  $u_{rms}(N_p = 1) = u_{rms,max} \approx 2.2$  m/s (figure B.13*a*). In a second step, particle velocities were averaged over  $N_p$  measured data points, followed by an evaluation of the *rms* of the velocity fluctuations ( $u_{rms}(N_p)$ ). The results (figure B.13*b*) were approximated by a logarithmic

expression:

$$u_{rms}/u_{rms,max} = 1 - \mathcal{K}_1 \ln(N_p)^{\mathcal{K}_2} \quad \{N_p \in \mathbb{Z}^+ : 1 \leq N_p \leq 100\} \quad (\text{B.2})$$

Eq. (B.2) is valid up to  $N_p \approx 100$  and the empirical constants  $\mathcal{K}_1$  and  $\mathcal{K}_2$  are a function of:

$$\mathcal{K}_1, \mathcal{K}_2 = f_1(f, Tu, T_{uu}, \dots) \quad (\text{B.3})$$

The derived relationship was also confirmed using virtual phase-detection probe signals of synthetic particles from Kramer et al. (2019) (figure B.13c).